Local Residual Minimization Smoothing for Improving Convergence Behavior of Space-Time Domain Decomposition Method

Hanyu Li and Mary F. Wheeler

Abstract Space-time domain decomposition approaches are showing promising results in providing significant computational speedup by distributing computational resources based on error estimation. This paper develops a robust approach to improve the Newtonian convergence behavior by smoothing residuals during the pre-processing step. Our space-time method for nonlinear problems uses geometrical multigrid Newtonian continuation procedure to approach the true solution, for which the linear prolongation of the unknowns generates high frequency residuals, that hinders the global convergence. The smoothing algorithm searches for subdomains with high frequency residuals and solves a local problem with a fixed boundary conditions. By removing high frequency residuals before continuing the Newton method, the iterations start quadratic convergence sooner and approaches the true solution more efficiently.

1 Introduction

Complex multiphase flow and reactive transport in subsurface porous media is mathematically modeled by systems of nonlinear equations. Due to significant nonlinearity, solving such systems with Newton's method requires small time steps for stable numerical convergence, resulting in significant computational load. Our space-time domain decomposition method addresses this difficulty by allowing different time scales for different spatial subdomains of the system, thus distributing computing resources according to load requirements.

Hanyu Li
Oden Institute for Computational Engineering and Sciences, 201 E 24th St, Austin, TX 78712,
e-mail: `lihanyu234@utexas.edu`

Mary F. Wheeler
Oden Institute for Computational Engineering and Sciences, 201 E 24th St, Austin, TX 78712
e-mail: `mfw@oden.utexas.edu`

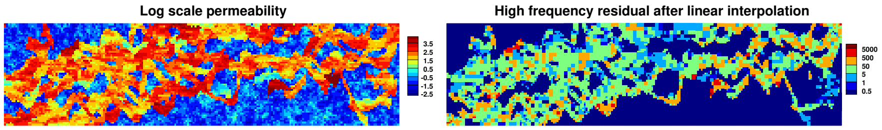

Fig. 1: High frequency residual after linear interpolation of multigrid method for rough coefficient cases

Many space-time domain decomposition approaches have been proposed in the past. To mention a few works, such as [1, 8, 9], space-time finite elements were introduced for elastodynamics with discontinuous Galerkin (DG) in time. The space-time method has also been applied to other systems such as reaction-diffusion problems, with different time discretization schemes [3, 10, 11, 12]. Regarding flow in porous media, [7] focused on linear single phase flow and transport problems where flow is naturally decoupled from advection-diffusion transport. In [17] a space-time approach for nonlinear coupled multiphase flow and transport problems on a static grid using an enhanced velocity method is formulated, a MFE variant [2, 18, 20], where the continuity of fluxes at non-matching space-time interfaces was strongly enforced.

Although space-time domain decomposition methods can provide tremendous computational speedup, initiating such system properly has always been a challenge, especially for nonlinear problems with rough coefficients. The main issue is, for subdomains with local time steps being solved in parallel, initiating all the local time steps with the solution at the previous space-time slab, which is similar to the procedure in traditional time-stepping schemes, frequently leads to non-convergence. In [13] a geometric multigrid type of approach was adopted, which starts solving each space-time slab with the coarsest resolution and sequentially refines the mesh in certain subdomains to the finest resolution. After each refinement, the unknowns on the finer mesh are generated by linear interpolation (prolongation) of the solution on the coarse mesh and the Newton iteration continues. The sequential refinement provides an initial guess of the unknowns close enough to the true solution to prevent convergence failure. However, like all multigrid methods, the linear interpolation causes high frequency residuals to appear sporadically throughout the entire domain, especially for problems with rough coefficients. An example is shown in Fig.1. Here a flow in subsurface porous media problem with channelized permeability as coefficients is presented. The discontinuity of the permeability is clearly observed at the channel boundary. On the right hand side, we demonstrate the initial residual of a typical space-time slab after the prolongation step. The high frequency residuals colored in red appear sporadically throughout the system, typically on the channel boundary. As the Newton's method continues, the first few iterations focuses on reducing such high frequency residuals while not much effort is devoted to the rest of the system. Therefore, it is critical to remove these high frequency residuals before continuing the Newton iteration, to harness the full potential of space-time domain decomposition.

In this paper, we introduce a local residual minimization algorithm to improve Newtonian convergence behavior of space-time geometric multigrid method. In Section 2, we present the model problem followed by the smoothing algorithm in Section 3. Results from numerical experiment using the proposed algorithm are discussed in Section 4. Summary of our findings follows in Section 5.

2 Flow model problem

We use miscible multiphase flow in porous media as the model problem due to its extensive nonlinearity imposing significant numerical convergence challenges. Since miscible flow involves multiple component coexisting in a single fluid phase, therefore we need to write the governing equation of the model in component form. A simplified version of such model is the black-oil model widely accepted in the petroleum engineering industry, which we use to demonstrate our numerical results.

To start off, assuming no dispersion, the conservation equation of a component existing in a given fluid phase is stated as follow

$$\frac{\partial}{\partial t}(\varphi \rho_\alpha \xi_{c\alpha} s_\alpha) + \nabla \cdot (\xi_{c\alpha} \boldsymbol{u}_\alpha) = q_{c\alpha} + r_{c\alpha} . \tag{1}$$

Here, φ is the porosity. ρ_α, s_α and $\boldsymbol{u}_\alpha$ are the density, saturation and velocity of the fluid phase. $\xi_{c\alpha}$ is the fraction of component c included in phase α, in either mass or molar basis. $q_{c\alpha}$ is the source/sink and $r_{c\alpha}$ is the increase/decrease rate of component c in phase α due to phase changes. The rate of phase change and mass/molar fraction of component c obeys the following constrain.

$$\sum_\alpha r_{c\alpha} = 0 , \tag{2}$$

$$\sum_c \xi_{c\alpha} = 1, \ \xi_{c\alpha} \geq 0 . \tag{3}$$

We sum Eqn.(1) over the total number of phases (N_p) to acquire the component mass conservation equation as

$$\frac{\partial}{\partial t}\left(\varphi \sum_\alpha \rho_\alpha \xi_{c\alpha} s_\alpha\right) + \nabla \cdot \left(\sum_\alpha \xi_{c\alpha} \boldsymbol{u}_\alpha\right) = \sum_\alpha q_{c\alpha} . \tag{4}$$

To simplify the notation, let us define the component concentration and flux in a given phase by $n_{c\alpha} = \rho_\alpha \xi_{c\alpha} s_\alpha$ and $\boldsymbol{u}_{c\alpha} = \xi_{c\alpha} \boldsymbol{u}_\alpha$ while the total component concentration as $N_c = \sum_\alpha n_{c\alpha}$. Then we can rewrite Eqn.(4) as

$$\frac{\partial}{\partial t}\left(\varphi \sum_\alpha n_{c\alpha}\right) + \nabla \cdot \left(\sum_\alpha \boldsymbol{u}_{c\alpha}\right) = \sum_\alpha q_{c\alpha} . \tag{5}$$

The boundary and initial conditions are

$$\boldsymbol{u}_\alpha \cdot \boldsymbol{\nu} = 0 \quad on\ \partial\Omega \times J \ , \tag{6}$$

$$\begin{cases} p_\alpha = p_\alpha^0 \\ N_c = N_c^0 \end{cases} \quad at\ \Omega \times \{t = 0\} \ , \tag{7}$$

where $J = (0, T]$ is the time domain of interest and Ω is the spatial domain. The phase velocity is given by Darcy's law as

$$\boldsymbol{u}_\alpha = -K\rho_\alpha \frac{k_{r\alpha}}{\mu_\alpha}(\nabla p_\alpha - \rho_\alpha \boldsymbol{g}) \ , \tag{8}$$

in which K is the absolute permeability while $k_{r\alpha}$, μ_α and p_α are relative permeability, viscosity and pressure for the given fluid phase. The relative permeability and capillary pressure are functions of phase saturations.

In complex compositional simulations, the saturations are estimated by concentrations after finding the equilibrium hydrocarbon component distribution. This procedure is called flash vaporization calculation and readers can refer to [16] for details. In this paper, we avoid such complexity and use the black-oil model as the simplified compositional model to further introduce our concept. The black-oil model allows a maximum number of three phases in the system, namely oleic, aqueous and gaseous. The components contained within are water, hydrocarbon oil which mainly consists of heavy non-volatile molecules and hydrocarbon gas which mostly includes light volatile molecules. Consequently the hydrocarbon gas can exist as either free gas or dissolved gas in the oleic phase. This results in the following relations on the component fractions:

$$\begin{aligned} &\xi_{1o} + \xi_{3o} = 1, \quad \xi_{2o} = 0 \\ &\xi_{1w} = 0, \quad \xi_{2w} = 1, \quad \xi_{3w} = 0 \\ &\xi_{1g} = 0, \quad \xi_{2g} = 0, \quad \xi_{3g} = 1. \end{aligned} \tag{9}$$

ξ_{3o} is commonly referred to as the solution gas-oil ratio and is usually a function of pressure, but it remains constant after the oleic phase reaches the bubble point pressure. We remark that if the hydrocarbon oil component also contains some medium weight molecules and thus is able to vaporize into the gaseous phase, then we obtain the volatile oil model. The dissolved gas causes the oleic phase to swell thus decreasing its density. Considering the hydrocarbon oil component itself is slightly compressible, such swelling effect can be described by the following equation:

$$\rho_o = \rho_{o,std} \cdot (e^{-c_o p_o} + \beta\xi_{3o})^{-1} \ . \tag{10}$$

The aqueous and gaseous phase, which contain only water and the hydrocarbon gas component, are slightly compressible and fully compressible, respectively. Therefore, the two phase densities are given as follow:

$$\rho_w = \rho_{w,std} \cdot e^{c_w p_w} \ , \tag{11}$$

$$\rho_g = \rho_{g,std} \cdot c_g p_g \ . \tag{12}$$

Then saturations can be related to concentrations by

$$\begin{cases} s_o = \dfrac{N_1}{\rho_o(1-\xi_{3o})} \\ s_w = \dfrac{N_2}{\rho_w} \\ s_g = \dfrac{1}{\rho_g}\left(N_3 - N_1 \dfrac{\xi_{3o}}{1-\xi_{3o}}\right) \end{cases} , \tag{13}$$

with the following constrain

$$\sum_\alpha s_\alpha = 1, \ s_\alpha \geq 0 \ . \tag{14}$$

Let $\boldsymbol{V} = H(div;\Omega),\ W = L^2(\Omega)$ with $\boldsymbol{V}_h$ and W_h be the finite dimensional subspaces. Let $J_n = (t_n, t_{n+1}]$ be the nth partition of the time domain of interest. Then for each space-time slab $J_n \times \Omega$, we define velocity and pressure/saturation spaces as, for any element $E = F_E \times T_E$

$$\boldsymbol{V}_h^n = \left\{ \boldsymbol{v} \in L^2\Big(J_n; H(div;\Omega)\Big) : \boldsymbol{v}(\cdot,\boldsymbol{x})\Big|_{F_E} \in \boldsymbol{V}_h,\ \boldsymbol{v}(t,\cdot)\Big|_{T_E} = \sum_{a=1}^{l} \boldsymbol{v}_a t^a \ \&\ \boldsymbol{v}_a \in \boldsymbol{V}_h \right\},$$

$$W_h^n = \left\{ w \in L^2\Big(J_n; L^2(\Omega)\Big) : w(\cdot,\boldsymbol{x})\Big|_{F_E} \in W_h,\ w(t,\cdot)\Big|_{T_E} = \sum_{a=1}^{l} w_a t^a \ \&\ w_a \in W_h \right\}.$$

Functions in $\boldsymbol{V}_h^n$ and W_h^n along time dimension are represented by polynomials with degrees up to l. We formulate the space-time enhanced velocity variational formulation as: find $\boldsymbol{u}_{\alpha,h}^n, \tilde{\boldsymbol{u}}_{\alpha,h}^n \in \boldsymbol{V}_h^n$ and $p_{\alpha,h}^n, s_{\alpha,h}^n, \xi_{c\alpha,h}^n \in W_h^n$ such that

$$\begin{aligned} \int_{J_n}\int_\Omega \partial_t\Big(\varphi \sum_\alpha n_{c\alpha,h,\tau}^n\Big) w + \int_{J_n}\int_\Omega \Big(\nabla \cdot \sum_\alpha \boldsymbol{u}_{up,c\alpha,h}^n\Big) w \\ = \int_{J_n}\int_\Omega \Big(\sum_\alpha q_{c\alpha}\Big) w \quad \forall w \in W_h^n \ , \end{aligned} \tag{15}$$

$$\int_{J_n}\int_\Omega K^{-1} \tilde{\boldsymbol{u}}_{\alpha,h}^n \cdot \boldsymbol{v} = \int_{J_n}\int_\Omega p_{\alpha,h}^n \nabla \cdot \boldsymbol{v} \quad \forall \boldsymbol{v} \in \boldsymbol{V}_h^n \ , \tag{16}$$

$$\int_{J_n}\int_\Omega \boldsymbol{u}_{\alpha,h}^n \cdot \boldsymbol{v} = \int_{J_n}\int_\Omega \lambda_\alpha \tilde{\boldsymbol{u}}_{\alpha,h}^n \cdot \boldsymbol{v} \quad \forall \boldsymbol{v} \in \boldsymbol{V}_h^n \ . \tag{17}$$

The phase mobility ratio in Eqn.(17) is defined as

$$\lambda_\alpha = \rho_\alpha \frac{k_{r\alpha}}{\mu_\alpha} \ , \tag{18}$$

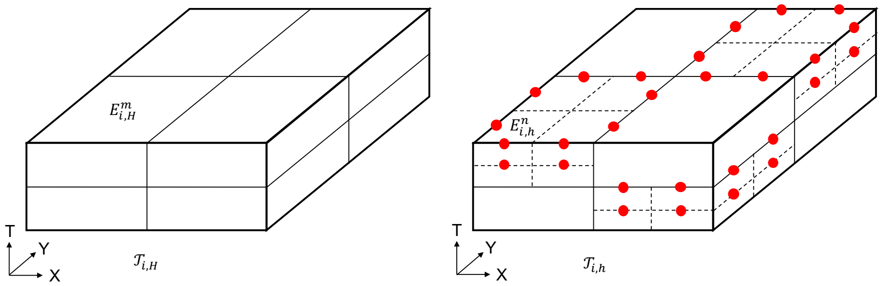

Fig. 2: Coarse and refined partition of subdomain $I_i \times \Omega_i$ with boundary interpolation nodes (red circles)

and $\boldsymbol{u}^n_{up,\alpha,h}, \boldsymbol{u}^n_{up,c\alpha,h}$ are the upwind velocities calculated by

$$\int_{J_n}\int_{\Omega} \boldsymbol{u}^n_{up,\alpha,h} \cdot \boldsymbol{v} = \int_{J_n}\int_{\Omega} \lambda^*_{\alpha} \tilde{\boldsymbol{u}}^n_{\alpha,h} \cdot \boldsymbol{v} \quad \forall \boldsymbol{v} \in \boldsymbol{V}^n_h \ , \tag{19}$$

$$\int_{J_n}\int_{\Omega} \boldsymbol{u}^n_{up,c\alpha,h} \cdot \boldsymbol{v} = \int_{J_n}\int_{\Omega} \xi^*_{c\alpha} \boldsymbol{u}^n_{up,\alpha,h} \cdot \boldsymbol{v} \quad \forall \boldsymbol{v} \in \boldsymbol{V}^n_h \ . \tag{20}$$

The additional auxiliary phase fluxes $\tilde{\boldsymbol{u}}^n_{\alpha,h}$ is used to avoid inverting zero phase relative permeability [15]. Calculation of the upwind properties $(\lambda^*_{\alpha}, \xi^*_{c\alpha})$ is done by using saturations and component fractions from the grid cell on the upwind direction of the pressure gradient. We choose pressure and saturations as primary unknowns to solve. In case of phase disappearance, the solution gas-oil ratio (ξ_{3o}) needs to replace gaseous phase saturation (s_g) as the new primary unknown and vice versa.

3 Local residual minimization

Previous work regarding residual smoothing mainly involved linear problems with rough coefficients. Such pre-processing serves as a preconditioner for iterative linear solvers, such as the conjugate gradient method, and reduces their iteration counts significantly. In [19], an energy minimization method was introduced, which solves for a coarse basis function that minimizes the energy functional on the fine grid. However, direct application of such approach on nonlinear transport is problematic since no energy functional can be constructed due to the degenerate coefficients. Therefore we propose the local residual minimization approach.

Consider $J_n \times \Omega$ as an union of some non-overlapping subdomains $\{I_i \times \Omega_i\}$, namely $J_n \times \Omega = \cup_i (I_i \times \Omega_i)$, where $I_i = (\tau_i, \tau_{i+1}]$ is a sub-interval of $J_n = (t_n, t_{n+1}]$ and Ω_i is a subdomain of Ω. Now let $\mathcal{T}_{i,H}$ be a coarse rectangular partition of $I_i \times \Omega_i$, $E^m_{i,H} = T^m_i \times F^m_i$ be a space-time element in such partition with $T^m_i = (\tau^m_{i,0}, \tau^m_{i,1}]$. Consider $\mathcal{T}_{i,H}$ to be partially refined that results in a finer rectangular partition $\mathcal{T}_{i,h}$ with elements $E^n_{i,h}$. We define the linear interpolation of a piecewise constant function (pressure and saturation) in space-time slab as f_ζ. We then construct the local problem as follow:

$$\int_{E^m_{i,H}} \sum_\alpha \left(\partial_t\left(\varphi n^n_{c\alpha,h,\tau}\right) + \nabla\cdot \boldsymbol{u}^n_{up,c\alpha,h} - q_{c\alpha}\right) w = 0 \qquad (21)$$
$$\forall E^m_{i,H} = \cup_{E^n_{i,h}\subsetneq E^m_{i,H}} E^n_{i,h}\ ,$$

subject to

$$\begin{cases} p_\alpha = p_{\alpha,\zeta} \\ s_\alpha = s_{\alpha,\zeta} \end{cases} \quad on\ \partial E^m_{i,H}\ . \qquad (22)$$

Fig.2 demonstrates the two partitions and the boundary interpolation nodes necessary for solving the local system. The boundary nodes appear on the top of the time level due to the discontinuous Galerkin of order zero discretization scheme.

If the interpolated pressure and saturations on the boundary is exact, then Eqn.(21) is well-posed and provides an unique solution that matches the global solution on the local subdomain. Unfortunately, providing exact boundary saturations by linear interpolation of the coarse solution is hardly achievable in nonlinear transport. The main reason being the transport and advection-diffusion process are closely coupled, making the variations of the pressure field across different grid resolutions to have a strong influence on transport flow equation. Therefore, the local problem tends to be ill-posed. In response, we rewrite Eqn.(21) into a minimization problem as follow:

$$\min_{p_{\alpha,h}, s_{\alpha,h}} \left\{ \left\| \int_{E^m_{i,H}} \sum_\alpha \left(\partial_t\left(\varphi n^n_{c\alpha,h,\tau}\right) + \nabla\cdot \boldsymbol{u}^n_{up,c\alpha,h} - q_{c\alpha}\right) w \right\|_\infty \right\} \qquad (23)$$
$$\forall E^m_{i,H} = \cup_{E^n_{i,h}\subsetneq E^m_{i,H}} E^n_{i,h}\ .$$

Since the goal of the minimization is only to remove the high frequency residuals (smoothing), to prevent over-working the problem, the algorithm is stopped once reaching the average background residual instead of the absolute minimum.

Like solving the global problem, we use Newton's method to reduce the high frequency local residual. However, with a reduced problem size providing less constraint on the system, a "soft" Jacobian is likely to produce a solution outside the acceptable range (eg. saturations must be in $[0, 1]$). Therefore, we apply the line search algorithm introduced in [14] to prevent divergence during the Newton iteration. Line search scales back the update when the Jacobian appears to be too "soft", by setting the update direction orthogonal to the post update residual.

4 Numerical results

We apply the SPE10 dataset [4] to conduct our numerical experiments. The fluid data are listed in Table.1. The solution gas-oil ratio is estimated by

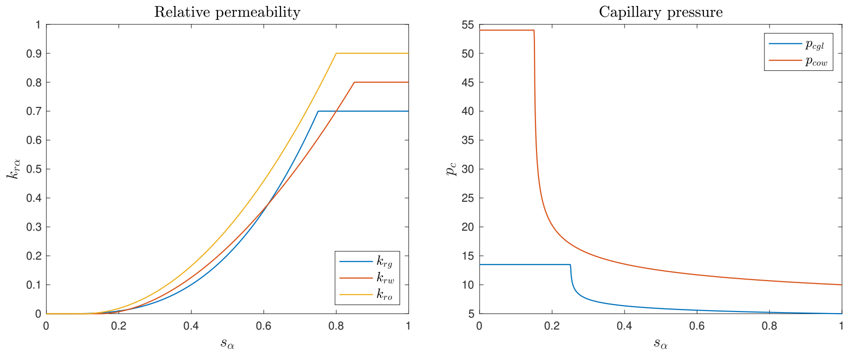

Fig. 3: Relative permeability (left) and capillary pressure (right) curve for numerical experiment

Table 1: Fluid data for numerical experiment

Parameter	Value	Unit
Gas compressibility (c_g)	5.0×10^{-2}	psi^{-1}
Oil compressibility (c_o)	1.0×10^{-4}	psi^{-1}
Water compressibility (c_w)	3.0×10^{-6}	psi^{-1}
Gas viscosity (μ_g)	0.03	cp
Oil viscosity (μ_o)	3.0	cp
Water viscosity (μ_w)	1.0	cp
Gas standard density ($\rho_{g,std}$)	0.1	lb/ft^3
Oil standard density ($\rho_{o,std}$)	53	lb/ft^3
Water standard density ($\rho_{w,std}$)	64	lb/ft^3
Solution gas-oil ratio exponent (n_{rs})	-1.5×10^{-4}	
Bubble point pressure (p_b)	3000.0	psi

$$\xi_{3o} = \begin{cases} 1 - e^{n_{rs} p_o} & if\ p_o < p_b \\ 1 - e^{n_{rs} p_b} & if\ p_o \geq p_b \end{cases} , \tag{24}$$

with n_{rs} and p_b being the exponent and bubble point pressure respectively. We take $\beta = 2$ for Eqn.(10) to calculate oil density. For nonlinear transport, we use Brooks-Corey model illustrated in Fig.3 for both relative permeability and capillary pressure, which is described by Eqn.(25) and (26):

$$\begin{cases} k_{rg} = k_{rg}^0 \left(\dfrac{s_g - s_{gr}}{1 - s_{gr} - s_{or} - s_{wr}} \right)^{n_g} \\ k_{ro} = k_{ro}^0 \left(\dfrac{s_o - s_{or}}{1 - s_{gr} - s_{or} - s_{wr}} \right)^{n_o} \\ k_{rw} = k_{rw}^0 \left(\dfrac{s_w - s_{wr}}{1 - s_{gr} - s_{or} - s_{wr}} \right)^{n_w} \end{cases} , \tag{25}$$

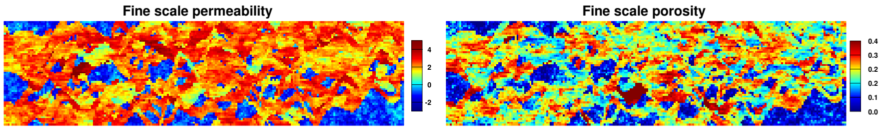

Fig. 4: Channelized fine scale permeability (left) and porosity (right) distribution

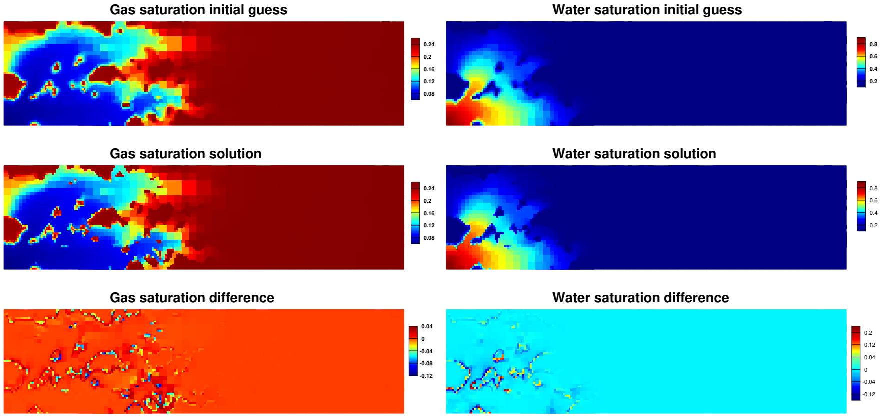

Fig. 5: Difference between saturation initial guess and solution without local residual minimization

$$\begin{cases} p_{cgl} = p_{en,cgl}\left(\dfrac{1 - s_{or} - s_{wr}}{s_o + s_w - s_{or} - s_{wr}}\right)^{l_{cgl}} \\ p_{cow} = p_{en,cow}\left(\dfrac{1 - s_{wr}}{s_w - s_{wr}}\right)^{l_{cow}} \end{cases} . \tag{26}$$

The endpoint values for relative permeability are $k^0_{rg} = 0.7$, $k^0_{ro} = 0.9$, $k^0_{rw} = 0.8$, $s_{gr} = 0.05$, $s_{or} = 0.1$, $s_{wr} = 0.15$ and the exponents are $n_g = 2.5$, $n_o = 2.0$, $n_w = 1.8$. There are capillary pressures on both water-oil and gas-liquid interfaces. The entry pressures are $p_{en,cow} = 10\ psi$, $p_{en,cgl} = 5\ psi$ and the exponents are $l_{cow} = 0.25$, $l_{cgl} = 0.15$. The reservoir size is $56ft \times 216ft \times 1ft$. We place a water rate specified injection well at the bottom left corner and a pressure specified production well at the upper right corner. The water injection rate is $1\ ft^3/day$ and production pressure is 2000 psi. Furthermore, the initial pressure, gas saturation and water saturation are set to be 2000 psi, 0.25 and 0.15 respectively.

The experiment uses the bottom layer of the SPE10 dataset as petrophysical property input. The fine scale data are shown in Fig.4 with clear discontinuity at the channel boundary. We use the algorithm described in [13] to solve the system. The number of refinement levels is set to three in both space and time and the refinement ratio is set to 2 uniformly. A numerical homogenization algorithm introduced in [5] and [6] is used to compute coarse resolution data.

The main cause of high frequency residual is the inaccurate initial estimate of saturations due to the discontinuous nature of the solution. An sample snapshot during

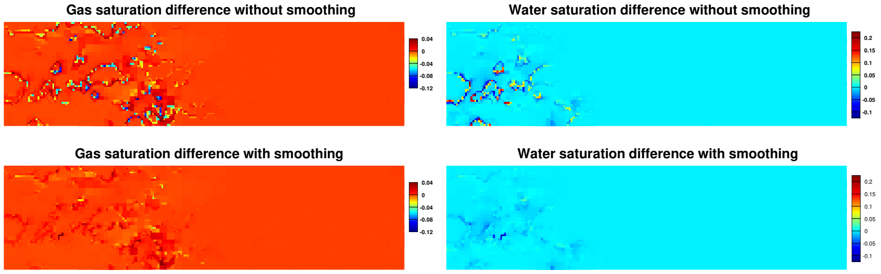

Fig. 6: Difference between saturation initial guess and solution with and without local residual minimization

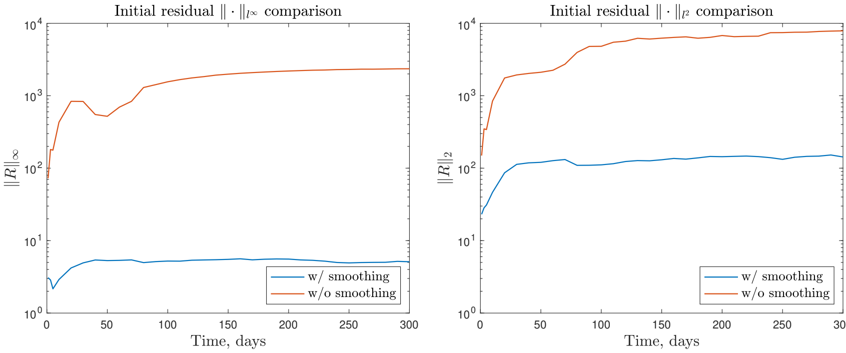

Fig. 7: l_∞ and l_2 norm of initial residual with and without local residual minimization

the numerical experiment is shown in Fig.5. Here, the initial guess of the saturations is compared to their respective final solutions and the difference between the two is calculated. We observe major discrepancies along the channel boundary since the saturation solution is discontinuous in such regions while the linear interpolation of the coarse solution provides a continuous transition. Now we apply the local residual minimization algorithm as a pre-processing step and compare the saturation difference to the same quantity without smoothing. The result is illustrated in Fig.6. We observe that the discrepancies along the channel boundary has been reduced significantly. Most part of the system shows no sign of inconsistency between the initial guess and the solution. Some mismatch still exist, typically in regions with complex channel structure. Minimizing local residuals in these regions is unstable since a clear flow direction cannot be determined when only a small subdomain of the system is provided. Applying an oversampling technique could improve the stability of the minimization process.

We also quantifies the reduction in initial residual when the Newton iteration continues after grid refinement and the result is demonstrated in Fig.7. We observe that by applying the minimization algorithm as a smoothing pre-process, the initial residual has been reduced by approximately two orders of magnitude. As a result, the global system enters quadratic convergence region sooner during Newton iteration and therefore improves convergence behavior. The number of iterations required to achieve convergence is reduced by roughly 40%.

5 Conclusions

In this paper, a space-time compositional model has been considered and we are unaware of any such computations. We introduce the local residual minimization algorithm as a pre-processing step for geometric multigrid type methods to remove high frequency residuals after grid refinement. The minimization is approached by solving the same global physical system using Newton's method in the local subdomain with boundary conditions set to linear interpolation of the coarse scale solution before mesh refinement. The iteration is terminated once the residual in the subdomain reaches global background residual instead of the absolute minimum, to prevent over-working the ill-posed local problem. Results from numerical experiment using a black-oil model is presented. We observe that after residual smoothing, the difference between saturation initial guess and solution is diminished significantly. The initial residual norm has been reduced by approximately 2 orders of magnitude. Such improvement facilitates the Newton's method to enter quadratic convergence region and therefore cuts the number of iterations required to achieve nonlinear convergence by 40%. The algorithm performance in regions with complex coefficient structure is sub-optimal, which can be improved by applying over-sampling techniques.

References

1. R. Abedi, B. Petracovici, and R.B. Haber. A space–time discontinuous galerkin method for linearized elastodynamics with element-wise momentum balance. *Computer Methods in Applied Mechanics and Engineering*, 195:3247–3273, May 2006.
2. Y. Amanbek, G. Singh, G. Pencheva, and M.F. Wheeler. Error indicators for incompressible darcy flow problems using enhanced velocity mixed finite element method. *Computer Methods in Applied Mechanics and Engineering*, 363:112884, May 2020.
3. M. Bause, F.A. Radu, and U. Köcher. Space-time finite element approximation of the biot poroelasticity system with iterative coupling. *Computer Methods in Applied Mechanics and Engineering*, 320:745–768, June 2017.
4. M.A. Christie and M.J. Blunt. Tenth spe comparative solution project: A comparison of upscaling techniques. *SPE Reservoir Evaluation and Engineering*, 4(04):308–317, Aug 2001.
5. E. Chung, Y. Efendiev, and T.Y. Hou. Adaptive multiscale model reduction with generalized multiscale finite element methods. *Journal of Computational Physics*, 320:69–95, Sept 2016.
6. Y. Efendiev and T.Y. Hou. *Multiscale finite element methods: theory and applications*, volume 4. Springer Science and Business Media, 2009.
7. T. Hoang, C. Japhet, M. Kern, and J.E. Roberts. Space-time domain decomposition for advection–diffusion problems in mixed formulations. *Mathematics and Computers in Simulation*, 137:366–389, July 2017.
8. T.J.R. Hughes and G.M. Hulbert. Space-time finite element methods for elastodynamics: Formulations and error estimates. *Computer Methods in Applied Mechanics and Engineering*, 66(3):339–363, Feb 1988.

9. G.M. Hulbert and T.J.R. Hughes. Space-time finite element methods for second-order hyperbolic equations. *Computer Methods in Applied Mechanics and Engineering*, 84(3):327–348, Dec 1990.
10. U. Köcher and M. Bause. Variational space–time methods for the wave equation. *Journal of Scientific Computing*, 61(2):424–453, Nov 2014.
11. D. Krause and R Krause. Enabling local time stepping in the parallel implicit solution of reaction–diffusion equations via space-time finite elements on shallow tree meshes. *Applied Mathematics and Computation*, 277:164–179, Mar 2016.
12. U. Langer, S.E. Moore, and M. Neumüller. Space–time isogeometric analysis of parabolic evolution problems. *Computer Methods in Applied Mechanics and Engineering*, 306:342–363, July 2016.
13. H. Li, W.T. Leung, and M.F. Wheeler. Sequential local mesh refinement solver with separate temporal and spatial adaptivity for non-linear two-phase flow problems. *Journal of Computational Physics*, 403:109074, Feb 2020.
14. H. Matthies and G. Strang. The solution of nonlinear finite element equations. *International Journal for Numerical Methods in Engineering*, 14(11):1613–1626, Dec 1979.
15. M. Peszyńska, M.F. Wheeler, and I. Yotov. Mortar upscaling for multiphase flow in porous media. *Computational Geosciences*, 6(1):73–100, Mar 2006.
16. G. Singh and M.F. Wheeler. Compositional flow modeling using a multi-point flux mixed finite element method. *Computational Geosciences*, 20:421–435, Oct 2015.
17. G. Singh and M.F. Wheeler. A space-time domain decomposition approach using enhanced velocity mixed finite element method. *Journal of Computational Physics*, 374:893–911, Dec 2018.
18. S.G. Thomas and M.F. Wheeler. Enhanced velocity mixed finite element methods for modeling coupled flow and transport on non-matching multiblock grids. *Computational Geosciences*, 15(4):605–625, Sept 2011.
19. W. L. Wan, T. F. Chan, and B. Smith. An energy-minimizing interpolation for robust multigrid methods. *SIAM Journal of Scientific Computing*, 21(4):1632–1649, Dec 1998.
20. J.A. Wheeler, M.F. Wheeler, and I. Yotov. Enhanced velocity mixed finite element methods for flow in multiblock domains. *Computational Geosciences*, 6:315–332, Jan 2002.

Part II
Talks in Minisymposia